

Dynamics of reorientations and reversals of large-scale flow in Rayleigh–Bénard convection

P. K. MISHRA¹†, A. K. DE², M. K. VERMA¹ AND V. ESWARAN³

¹Department of Physics, Indian Institute of Technology, Kanpur 208016, India

²Department of Mechanical Engineering, Indian Institute of Technology, Guwahati 781039, India

³Department of Mechanical Engineering, Indian Institute of Technology, Kanpur 208016, India

(Received 13 March 2010; revised 11 September 2010; accepted 13 September 2010;
first published online 16 December 2010)

We present a numerical study of the reversals and reorientations of the large-scale circulation (LSC) of convective fluid in a cylindrical container of aspect ratio one. We take Prandtl number to be 0.7 and Rayleigh numbers in the range from 6×10^5 to 3×10^7 . It is observed that the reversals of the LSC are induced by its reorientation along the azimuthal direction, which are quantified using the phases of the first Fourier mode of the vertical velocity measured near the lateral surface in the midplane. During a ‘complete reversal’, the above phase changes by around 180° , leading to reversals of the vertical velocity at all the probes. On the contrary, the vertical velocity reverses only at some of the probes during a ‘partial reversal’ with phase change other than 180° . Numerically, we observe rotation-led and cessation-led reorientations, in agreement with earlier experimental results. The ratio of the amplitude of the second Fourier mode and the first Fourier mode rises sharply during the cessation-led reorientations. This observation is consistent with the quadrupolar dominant temperature profile observed during the cessations. We also observe reorientations involving double cessation.

Key words: plumes/thermals, turbulent convection, turbulence simulation

1. Introduction

Turbulent convection is ubiquitous in nature and in many engineering applications. The Rayleigh–Bénard convection (RBC) in which fluid confined between two plates is heated from below and cooled on the top is an idealized yet an important paradigm for understanding convective turbulence. The dynamics of RBC is governed by two non-dimensional parameters: the Rayleigh number $R = \alpha \Delta T d^3 g / \nu \kappa$ and the Prandtl number $P = \nu / \kappa$, where d is the vertical height of the container, g is the acceleration due to gravity, ΔT is the temperature difference between the bottom and top plates, and α , κ and ν are the thermal heat expansion coefficient, thermal diffusivity and kinematic viscosity, respectively, of the fluid.

Krishnamurti & Howard (1981) performed experiments on water ($P \simeq 7.0$) and silicon oil ($P \sim 860$) and observed coherent roll structures, also known as ‘large-scale circulation’ (LSC), in the turbulent regime. Subsequently, Castaing *et al.* (1989) ascertained the existence of LSC in helium ($P \simeq 0.65$ – 1.5) contained in a cylindrical container. They proposed that coherent large-scale structures exist statistically only

† Email address for correspondence: kumarpk@iitk.ac.in

above a certain Rayleigh number ($R \simeq 10^8$). They also observed a low-frequency peak in the power spectrum of the temperature field. Xi, Lam & Xia (2004) studied the onset of large-scale coherent mean flow in RBC using shadowgraph and particle-image velocimetry techniques and showed that LSC is a result of the organization of plume motion.

Cioni, Ciliberto & Sommeria (1997) performed RBC experiments on mercury ($0.021 < P < 0.026$) and placed several thermistors along the azimuth of the cylinder. They deduced the presence of global circulation from the dipolar temperature distribution measured by the probes. The temperature fluctuations (after subtracting the mean) switched sign randomly in their experiment. Since the warmer fluid ascends from one side, and the cooler fluid descends from the other side of the apparatus, Cioni *et al.* (1997) deduced that the vertical velocity would also exhibit random ‘reversals’ in phase with the temperature fluctuations. This feature of convection has been studied extensively using theoretical, experimental and computational tools (see reviews by Kadanoff 2001; Ahlers, Grossmann & Lohse 2009). In this paper, we perform a computational investigation of the reversal dynamics of the LSC in a cylindrical geometry.

Cioni *et al.* (1997) computed the first Fourier mode of the measured temperature field. They observed that the amplitude of the first Fourier mode never vanishes, but the phase of the Fourier mode is highly variable. A phase change of π corresponds to the reversal of the flow. Cioni *et al.* (1997) also observed a low-frequency peak in the energy spectrum that corresponds to the circulation frequency of the large-scale flow inside the cylinder. Tsuji *et al.* (2005) performed an experiment with mercury contained in a cylindrical container for aspect ratios 1/2, 1 and 2 and found that the low frequency peak is absent for an aspect ratio of 1/2. Niemela *et al.* (2001) and Sreenivasan, Bershadskii & Niemela (2002) reported reversals in their convection experiments on helium. Brown, Nikolaenko & Ahlers (2005) and Brown & Ahlers (2006) performed similar experiments on water ($P = 4.38$) and measured the temperature field in the bulk using probes placed at 1/4, 1/2 and 3/4 height of the cylinder. They observed that the plane containing LSC exhibits diffusive and sometimes quick significant drift in the azimuthal direction with the angular change ($|\Delta\theta|$) ranging from small values to π , i.e. $\pi/4 < |\Delta\theta| < \pi$. This is called the ‘reorientation’ of the LSC. The reorientation of the flow can occur in two ways: (a) through rotation of the circulation plane without any major reduction of the circulation strength; (b) through ‘cessation’ of the circulation, followed by a restart in a randomly chosen new direction. Brown & Ahlers (2006) also computed the amplitude of the first Fourier mode and found it to be non-zero for rotation-led reorientations and close to zero during cessation-led reorientations. Xi, Zhou & Xia (2006) measured azimuthal motion of the LSC using particle-image velocimetry and studied reversals of the LSC. They observed ‘double cessation’ in their experiments. In a similar set of experiments, Xi & Xia (2007, 2008*a,b*) observed strong dependence of the azimuthal reorientations on the aspect ratio of the cylinder.

Qiu & Tong (2001) performed RBC experiments on water and computed temperature correlation functions. They reported a transition from random chaotic states to a correlated turbulent state at around $R_c \simeq 5 \times 10^7$. However, Sano, Wu & Libchaber (1989) report strongly correlated large-scale flow beyond $R_c \simeq 4 \times 10^7$ for helium gas ($P = 0.7$).

Various models have been proposed to understand the dynamical behaviour of the LSC. Sreenivasan *et al.* (2002) and Benzi (2005) proposed a stochastic model in which the reversal of the LSC was explained as noise-induced switching between

two metastable states. Araujo, Grossmann & Lohse (2005) attempted to explain the irregular cessation and subsequent reversal of the LSC using the force and thermal balance on a single plume modelled by coupled nonlinear equations related to the Lorenz equations. Brown & Ahlers (2007, 2008) proposed a stochastic model with the strength and the azimuthal orientation of the LSC being determined by two stochastic ordinary differential equations; this model appears to explain the experimental observations of cessation and reorientation. Villermaux (1995) proposed a model to explain the low frequency oscillations in the temperature signal in the bulk. His model assumes that the modes of the boundary layers interact through the slow moving large-scale circulation.

There are only a small number of computational studies on the reorientation or reversal of LSC. Stringano & Verzicco (2006) simulated convection in air ($P=0.7$) in a cylinder with an aspect ratio of 1/2 and observed a single roll breaking into two counter-rotating rolls stack vertically. Benzi & Verzicco (2008) performed a simulation of the fluid at $R=6 \times 10^5$ with white noise added to the heat equation and studied the statistical behaviour of the observed reversals. Breuer & Hansen (2009) studied RBC for infinite Prandtl number in a two-dimensional (2D) box and observed reversals of the LSC for very high R ($R=10^9$). There are other 2D numerical experiments in a box that report that the reversals of the LSC is due to cessations (see Hansen, Yuen & Kroening 1990, 1992) or due to the chaotic movement of rolls perpendicular to the roll axis (see Paul *et al.* 2010).

In this paper, we study the dynamics of reversals of convective structures using direct numerical simulation (DNS) of turbulent RBC for $P=0.7$ in a cylinder of aspect ratio one. We apply conducting boundary conditions on the top and bottom plates and adiabatic boundary conditions on the lateral walls of the container. No-slip boundary condition is applied on all the surfaces of the container. Our simulations indicate an LSC in the container. Furthermore, we observe rotation-led and cessation-led reorientations of the LSC similar to those observed in experiments. We compute the amplitudes and phases of the Fourier modes of the vertical velocity measured near the lateral wall in the midplane and establish that the dynamics of the LSC can be captured quite well by the low wavenumber Fourier modes.

The outline of the paper is as follows. We present our numerical method in §2. The results pertaining to the observation of the LSC and their reorientations are presented in §3. We conclude our results in §4.

2. Numerical method

We numerically simulate the convective flow in a cylinder. The Boussinesq approximation is assumed for the buoyancy in the fluid. The relevant non-dimensionalized dynamical equations for the fluid are

$$\frac{\partial \mathbf{u}}{\partial t} + (\mathbf{u} \cdot \nabla) \mathbf{u} = -\nabla \sigma + T \hat{\mathbf{z}} + \sqrt{\frac{P}{R}} \nabla^2 \mathbf{u}, \quad (2.1)$$

$$\frac{\partial T}{\partial t} + (\mathbf{u} \cdot \nabla) T = \frac{1}{\sqrt{PR}} \nabla^2 T, \quad (2.2)$$

$$\nabla \cdot \mathbf{u} = 0, \quad (2.3)$$

where $\mathbf{u} = (u_x, u_y, u_z)$ is the velocity field, T is the temperature field, σ is the deviation of pressure from the conduction state, $R = \alpha g(\Delta T) d^3 / \nu \kappa$ is the Rayleigh number, $P = \nu / \kappa$ is the Prandtl number, and $\hat{\mathbf{z}}$ is the buoyancy direction. Here ν and κ are the kinematic viscosity and thermal diffusivity respectively, d is the vertical height

R	$N_r \times N_\theta \times N_z$	Δ_{min}	Δ_{max}	l_{max}	η_h	N_{BL}	dt	Nu (comp)	$\langle \epsilon_c^u \rangle / \langle \epsilon_a^u \rangle$	$\langle \epsilon_c^T \rangle / \langle \epsilon_a^T \rangle$
6×10^5	$33 \times 49 \times 97$	0.007	0.02	0.064	0.057	9	0.001	7.6	0.93	1.26
6×10^5	$33 \times 90 \times 97$	0.006	0.017	0.035	0.057	9	0.001	7.4	0.93	1.34
8×10^6	$75 \times 96 \times 145$	0.003	0.011	0.033	0.025	7	0.001	15.1	1.00	1.33
8×10^6	$100 \times 120 \times 201$	0.002	0.008	0.026	0.025	9	0.0005	15.6	1.10	1.34
2×10^7	$100 \times 120 \times 201$	0.002	0.008	0.026	0.018	7	0.0005	22.1	1.12	1.35
2×10^7	$100 \times 180 \times 201$	0.002	0.007	0.017	0.018	7	0.0005	22.3	1.08	1.34
3×10^7	$100 \times 120 \times 201$	0.0018	0.008	0.026	0.016	6	0.0005	24.03	–	–

TABLE 1. N_r , N_θ and N_z are the number of grids along the radial, azimuthal and vertical directions of the cylindrical container; Δ_{min} and Δ_{max} are the minimum and maximum mean grid sizes; $l_{max} = \max(2\pi r/N_\theta)$; η_h is the Kolmogorov length scale calculated using the expression $\eta_h \simeq \pi(P^2/RNu)^{1/4}$; N_{BL} is the number of points inside the thermal boundary layer; dt is the time step; Nu (comp) is the Nusselt number obtained from the simulation; $\langle \epsilon_c^u \rangle$ ($=\nu \langle |\nabla \mathbf{u}|^2 \rangle$) and $\langle \epsilon_c^T \rangle$ ($=\kappa \langle |\nabla T|^2 \rangle$) are the numerically calculated viscous and thermal dissipation rates, respectively; and $\langle \epsilon_a^u \rangle$ ($=\nu^3(Nu-1)RP^{-2}/d^4$) and $\langle \epsilon_a^T \rangle$ ($=\kappa(\Delta T)^2Nu/d^2$) are the analytical values of viscous and thermal dissipation rates, respectively. The last two columns show $\langle \epsilon_c^u \rangle / \langle \epsilon_a^u \rangle$ and $\langle \epsilon_c^T \rangle / \langle \epsilon_a^T \rangle$.

of the container, and ΔT is the temperature difference between the bottom and top plates. For the non-dimensionalization we have used d as the length scale, $\sqrt{\alpha(\Delta T)gd}$ (free-fall velocity) as the velocity scale, and ΔT as the temperature scale. Consequently, $d/\sqrt{\alpha g \Delta T d}$ is the time scale of our simulation. The aspect ratio of the container is taken to be one. We confine our study to $P=0.7$, which is a typical Prandtl number for air.

The above non-dimensionalized equations (2.1)–(2.3) are solved numerically for a cylindrical geometry using a finite-difference scheme. The convective parts of the equations are discretized in cylindrical coordinates using the fourth-order central explicit scheme of Tam & Webb (1993) with enhanced spectral resolution. The diffusive part is discretized using the second-order central-difference scheme. For the time advancement, we use the second-order Adam–Bashforth scheme for the nonlinear terms and the Crank–Nicholson scheme for the diffusive terms. We perform simulations for Rayleigh numbers $R=6 \times 10^5$, 8×10^6 , 2×10^7 and 3×10^7 . A comparison with experimental results shows that these Rayleigh numbers are near the threshold of strong turbulence regimes (see Sano *et al.* 1989).

The cylinder volume is discretized into variable grids with finer resolution near the boundary layers. Since the boundary layers significantly affect the dynamics of the LSC in convective turbulence, it is necessary to resolve the regions near the top and bottom plates, and the lateral walls (see Stevens, Verzicco & Lohse 2010). In our simulations we choose uniform grids along the azimuthal direction and non-uniform grids along the radial and vertical directions. For the grid spacing, the Grötzbach condition (Grötzbach 1983) is used, according to which the mean grid size $\Delta = (r \Delta \theta \Delta r \Delta z)^{1/3}$ should be smaller than the Kolmogorov and thermal diffusion length scales. Note that the Kolmogorov length scale (η_h) is estimated using the formula $\eta_h \simeq \pi(P^2/(R Nu))^{1/4}$, where Nu is the Nusselt number. We also calculate the width of the thermal boundary layer using the formula $\delta_T \sim 1/(2Nu)$ and ensure that the number of grid points inside the boundary layer (N_{BL}) should be greater than 3–5. The number of grid points inside the thermal boundary layer is given in table 1, and they satisfy the above condition.

Our simulations satisfy the Grötzbach condition as the minimum of the mean grid size (Δ_{min}) is smaller than η_h (see table 1). Note however that the maximum grid size

$l_{max} = \max(2\pi r/N_\theta)$ is sometimes larger than η_h . To validate our code, we compare the numerically computed Nusselt numbers at two different grids (one more resolved than the other) and find that the Nusselt numbers for the two different grids are quite close. We also calculate the kinetic energy dissipation rate $\langle \epsilon_c^u \rangle$ ($=\nu \langle |\nabla \mathbf{u}|^2 \rangle$) and the thermal dissipation rate $\langle \epsilon_c^T \rangle$ ($=\kappa \langle |\nabla T|^2 \rangle$) using the numerical data and compare them with their theoretical estimates $\langle \epsilon_a^u \rangle$ ($=\nu^3(Nu-1)RP^{-2}/d^4$) and $\langle \epsilon_a^T \rangle$ ($=\kappa(\Delta T)^2 Nu/d^2$) (Shraiman & Siggia 1990). The ratios $\langle \epsilon_c^u \rangle / \langle \epsilon_a^u \rangle$ and $\langle \epsilon_c^T \rangle / \langle \epsilon_a^T \rangle$ are listed in table 1. Clearly, the numerical kinetic dissipation rate is quite close to its analytical counterpart, with the maximum difference at 12%. For the thermal dissipation, the numerical value always seems to be higher than the analytical value, with the maximum difference around 35%. However, note that the theoretical estimates of $\langle \epsilon_c^u \rangle$ and $\langle \epsilon_c^T \rangle$ are functions of the Nusselt number for which we substitute its numerically computed value. Our numerical results on dissipation rates appear to be less accurate compared with those by Stevens *et al.* (2010). Also, our numerical thermal dissipation rates are always larger than the theoretical estimate in contrast to those by Stevens *et al.* (2010), who report lower values compared with the corresponding theoretical estimate. The above discrepancies are probably due to the difference in the time-integration schemes and the spatial derivative schemes used by us and Stevens *et al.* (2010).

We use fixed time-step dt which is listed in table 1. Because of the computational complexity, the longest computer run for $R = 2 \times 10^7$ took approximately 45 days on 32 cores of the CHAOS cluster of IIT Kanpur. To ensure that the initial conditions do not affect our final results, we start every run with a conductive state modulated with random noise. We validate our numerical code by comparing our results with past numerical results. For example, our numerical results for the Nusselt number (Nu) for different Rayleigh numbers fit with a relation $Nu \simeq 0.143R^{0.297}$, which is in good agreement with the earlier numerical results of Stringano & Verzicco (2006) and Verzicco & Camussi (1999), and the experimental observations of Niemela *et al.* (2000). Similar to some of the earlier experiments (see Cioni *et al.* 1997; Brown *et al.* 2005; Brown & Ahlers 2006; Xi & Xia 2008*b*), we place ‘probes’ in the bulk and the boundary layers of the cylinder to record the time series of the velocity and temperature fields. The probes are located at $\theta = \theta_j = j\pi/4$ ($j = 0 : 7$), the vertical heights of $z = 0.02, 0.25, 0.5, 0.75, 0.98$, and the radial distances of $r = 0.15, 0.3, 0.48$ from the axis. The bottom and top probes are inside the thermal boundary layers. A schematic diagram of the probes in the middle plane is depicted in figure 1(*a*). The non-dimensional r.m.s. values of the velocity u_z^{rms} and the eddy turnover time ($T_{eddy} = 2d/u_z^{rms}$) for various R values are listed in table 2. Note that u_z^{rms} has been computed by taking the time average of $(1/8)(\sum_{i=1}^8 (u_z^i)^2)^{1/2}$ for the eight probes placed at $z = 0.5$ and $r = 0.48$. The eddy turnover time ranges from 26 to 10 free-fall times for the range of Rayleigh numbers studied in this paper; its value decreases with the increase in the Rayleigh number, consistent with the earlier results of Qiu & Tong (2001).

In the next section, we study the properties of the temperature and velocity time series, and relate them to the earlier experimental results on reversals of LSC.

3. Numerical results

3.1. Large-scale circulation

The time series measured by the probes of figure 1(*a*) carries the signature of the LSC as described below. Later, we will relate the reversals of the vertical velocity field to the reorientation of the LSC. In figures 1(*b*) and 1(*c*), we display the temperature

R	$N_r \times N_\theta \times N_z$	u_z^{rms}	T_{eddy}
6×10^5	$33 \times 49 \times 97$	0.078	26
6×10^5	$33 \times 90 \times 97$	0.083	24
8×10^6	$75 \times 96 \times 145$	0.118	17
8×10^6	$100 \times 120 \times 201$	0.107	19
2×10^7	$100 \times 120 \times 201$	0.185	11
2×10^7	$100 \times 180 \times 201$	0.174	12
3×10^7	$100 \times 120 \times 201$	0.201	10

TABLE 2. N_r , N_θ and N_z are the number of grids along the radial, azimuthal and vertical directions of the cylindrical container; u_z^{rms} is the r.m.s. value of the vertical speed of the flow; and $T_{eddy} = 2d/u_z^{rms}$ is the circulation time of the large-scale flow.

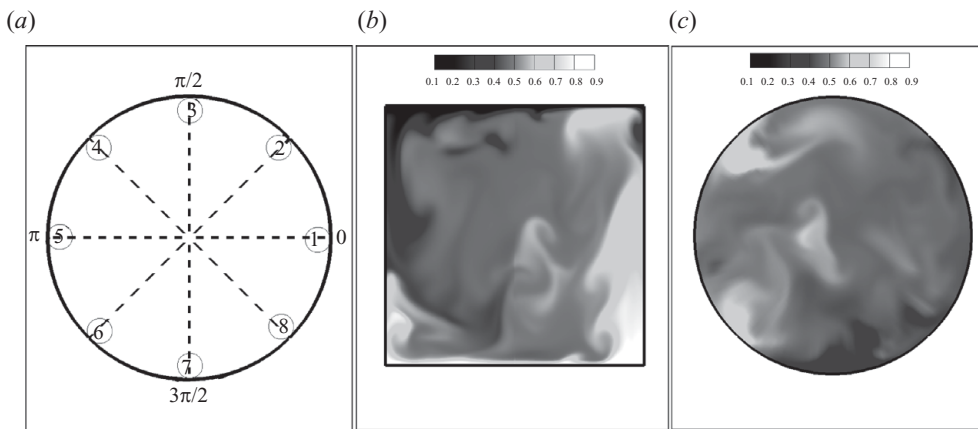


FIGURE 1. (a) Some of the velocity and temperature probes placed inside the cylinder. For most of our discussions in the paper, we use the probes at $z=0.5$, $r=0.48$ and $\theta = j\pi/4$ with $j=0 : 7$ shown in the figure. (b) Temperature profile in a vertical plane $\theta = 3\pi/4$ for $R = 2 \times 10^7$ on a $100 \times 120 \times 201$ grid. A hot plume ascends from the right wall and a cold plume descends from the left wall, confirming the presence of a large-scale structure. (c) Temperature profile in a horizontal section $z = 0.5$ for $R = 2 \times 10^7$ on a $100 \times 120 \times 201$ grid.

profiles for $R = 2 \times 10^7$ for a vertical plane ($\theta = 3\pi/4$) and the middle horizontal plane ($z = 0.5$), respectively. As supplementary material, we also provide two short movies, available at journals.cambridge.org/flm, depicting the flow behaviour for the above two sections. These figures and movies clearly indicate the presence of convective structures in the flow.

In figure 2(a–d), we plot the normalized autocorrelation $g_c(\tau) = \langle \delta T(t) \delta T(t + \tau) \rangle / \sigma_T^2$ at $\theta = 0$, $r = 0.48$, $z = 0.5$ for $R = 6 \times 10^5$, 8×10^6 , 2×10^7 and 3×10^7 , respectively. Here $\delta T(t) = T(t) - \bar{T}$ (\bar{T} is the mean temperature) and $\sigma_T^2 = \overline{T(t)^2} - (\bar{T})^2$, and time is measured in the units of eddy turnover time. The autocorrelation functions indicate two time scales in the system. Variations at the shorter time scale, shown in the insets, are due to the statistical return of the convective flow after one eddy turnover time or less (see table 1). For $R = 6 \times 10^5$ and 8×10^6 , the oscillations are somewhat irregular. However, for $R = 2 \times 10^7$ and 3×10^7 , the oscillations in the insets are quite regular and the oscillation time period of the autocorrelation function is around one eddy turnover time. This is also evident from the plot of the cross-correlation function of temperature between two azimuthally opposite probes placed at $\theta = 0$ and $\theta = \pi$, in

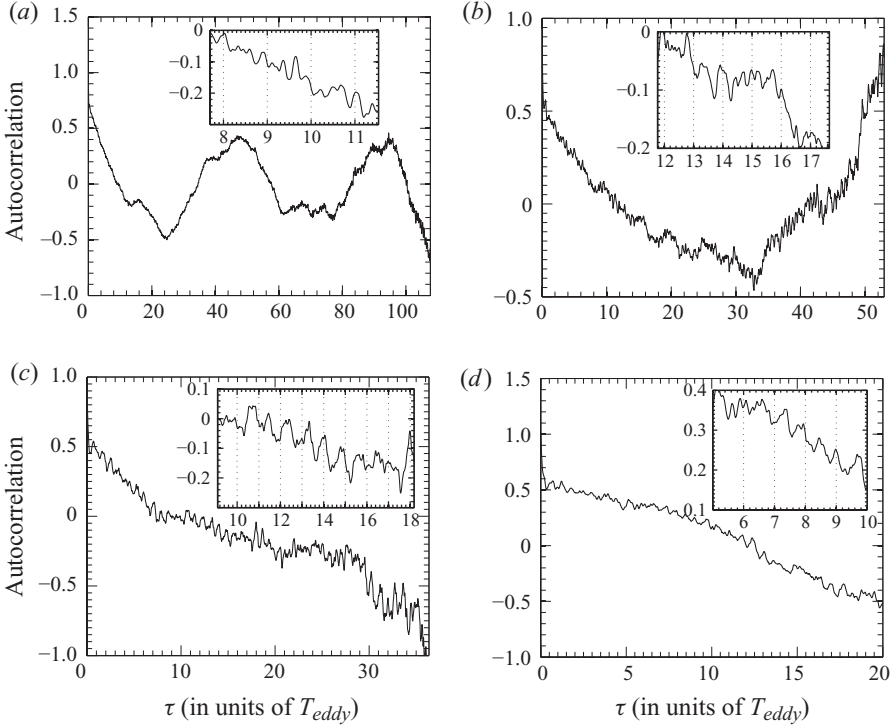


FIGURE 2. A plot of the autocorrelation function $g_c(\tau) = \langle \delta T(t) \delta T(t + \tau) \rangle / \sigma_T^2$ versus delay time τ (in units of large-eddy turnover time) for a probe at $r = 0.48$, $\theta = 0$ and $z = 0.5$: (a) $R = 6 \times 10^5$ on a $33 \times 49 \times 97$ grid, (b) $R = 8 \times 10^6$ on a $75 \times 96 \times 145$ grid, (c) $R = 2 \times 10^7$ on a $100 \times 120 \times 201$ grid and (d) $R = 3 \times 10^7$ on a $100 \times 120 \times 201$ grid. The insets show oscillations on the eddy turnover time scale.

the midplane ($z = 0.5$) at $r = 0.48$ (see figure 3). The cross-correlation function also shows oscillations with approximately one eddy turnover time as the time period, in general agreement with the observations of Castaing *et al.* (1989), Sano *et al.* (1989), Qiu & Tong (2001) and Xi *et al.* (2006). The above correlations are related to the peak in the power spectrum at a frequency corresponding to $1/T_{eddy}$. The peak in the spectrum however tends to be overshadowed by noise. Consequently, the correlation function appears to be a good tool for analysing these oscillations. Note that the autocorrelation studies tend to become strongly periodic when the LSC direction is locked, e.g. by a small tilt of the cylinder (Brown, Funfschilling & Ahlers 2007).

In addition to the above, we observe variations in the above autocorrelation and cross-correlation functions at much larger time scales. For $R = 6 \times 10^5$ (see figure 2a), there is a significant decrease in correlations till $\tau \simeq 23T_{eddy}$, after which correlations rise again to reach a maximum value at $\tau \simeq 46T_{eddy}$. These variations possibly correspond to the reorientations of the LSC. Similar features are observed for $R = 8 \times 10^6$ (see figure 2b). For $R = 2 \times 10^7$ and 3×10^7 , the autocorrelation functions decrease with time (see figure 2c,d). Incidentally, the cross-correlation function for $R = 2 \times 10^7$ shows minima at $\tau = 0$ and then at $\tau \approx 20T_{eddy}$, and a maximum at $\tau \approx 10T_{eddy}$, which possibly indicates reversals of the flow at $\tau \approx 10T_{eddy}$, and a reoccurrence at $\tau \approx 20T_{eddy}$. We could not perform longer statistics since the computer simulations of RBC flows for large Rayleigh numbers are computationally very expensive. The autocorrelation and cross-correlation function studies are inconclusive

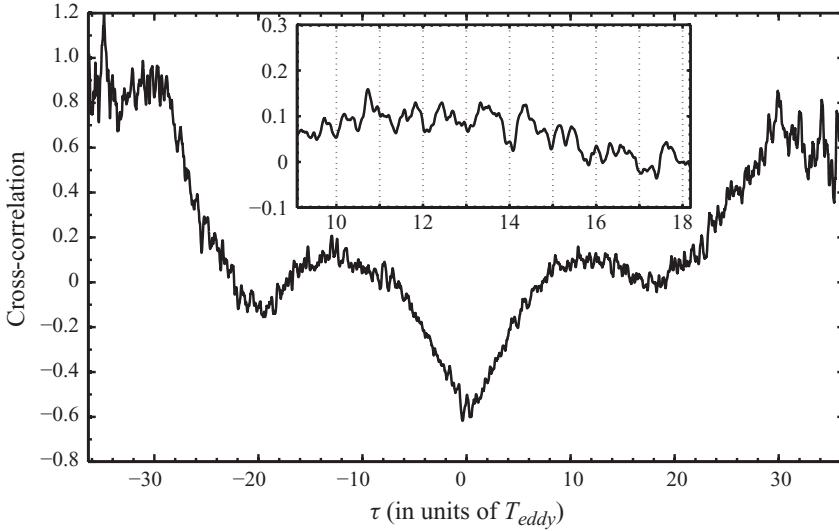


FIGURE 3. For $R = 2 \times 10^7$ on a $100 \times 120 \times 201$ grid, the cross-correlation function between the temperature measured at two azimuthally opposite probes at $\theta = 0$ and $\theta = \pi$ in the midplane at $r = 0.48$. The inset shows oscillations on the eddy turnover time scale.

due to averaging, yet the above observations indicate with some certainty that LSC exists in RBC. The reversal time could not be deduced from the present correlation functions. The presence of the LSC becomes more apparent when we study the time series of the velocity and temperature fields in the next section.

3.2. Measure of reorientations of LSC

The time series of the vertical velocity field for $R = 6 \times 10^5$, 8×10^6 , 2×10^7 recorded by the probes at $\theta_j = j\pi/4$ ($j = 0 : 7$), $r = 0.48$ and $z = 0.5$ are shown in figures 4, 5 and 6, respectively. Here time is measured in the units of the free-fall time ($d/\sqrt{\alpha g(\Delta T)d}$). The figures clearly show that vertical velocity at probes θ_j and $(\theta_j + \pi) \bmod 2\pi$ is clearly anti-correlated. These observations indicate the presence of a large-scale convective structure (see figure 1*b,c*). As shown in figures 4–6, the local mean value (in time) of the vertical velocity changes sign, and this feature is called ‘reversal’ of the LSC in the literature.

In the following discussions, we will show that the above-mentioned reversals are connected to the ‘reorientations’ of the LSC. To quantify the reorientations, we Fourier transform the vertical velocity field measured at $r = 0.48$ and $z = 0.5$. Note that these probes are near the lateral wall in the midplane. The velocity signal at a given probe can be expressed in terms of its Fourier transform as

$$u_j(t) = \sum_{k=-4}^4 \hat{u}_k \exp(ik\theta_j), \quad (3.1)$$

$$= \sum_{k=-4}^4 |\hat{u}_k| \exp(ik\theta_j + \delta_k), \quad (3.2)$$

$$= u_{mean} + \sum_{k=1}^4 2|\hat{u}_k| \cos(k\theta_j + \delta_k), \quad (3.3)$$

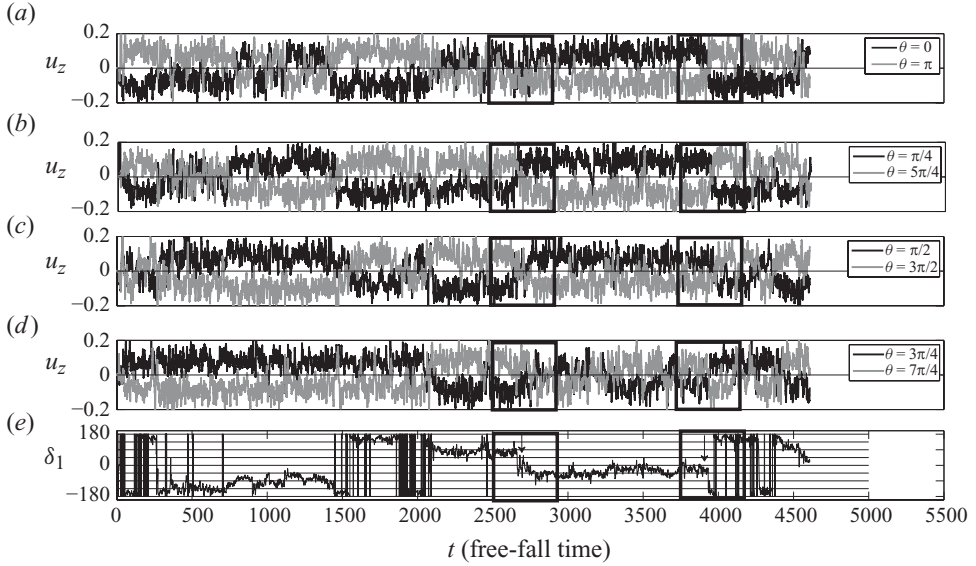


FIGURE 4. For $R = 6 \times 10^5$ on a $33 \times 49 \times 97$ grid, the time series of the vertical velocity measured by the probes at $z = 0.5$ (midplane), $r = 0.48$: (a) $\theta = 0$ and $\theta = \pi$, (b) $\theta = \pi/4$ and $\theta = 5\pi/4$, (c) $\theta = \pi/2$ and $\theta = 3\pi/2$ and (d) $\theta = 3\pi/4$ and $\theta = 7\pi/4$. (e) The time series of the phase of the first Fourier mode of the vertical velocity (δ_1). Time is measured in the units of the free-fall time $d/\sqrt{\alpha g \Delta T d}$. The arrows (inside boxed regions) in (e) indicate a partial reorientation ($\delta_1 \approx 135^\circ$) near $t \approx 2700$ and a complete reversal ($\delta_1 = 180^\circ$) near $t \approx 3900$.

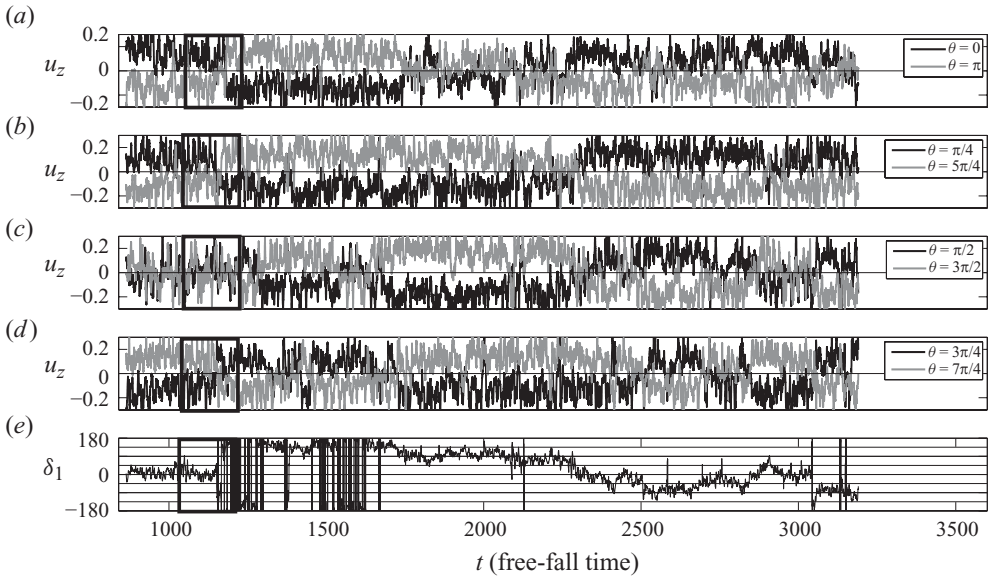


FIGURE 5. For $R = 8 \times 10^6$ on a $75 \times 96 \times 145$ grid, the time series of the vertical velocity measured by the probes at $z = 0.5$ (midplane) and $r = 0.48$, and the phase of the first Fourier mode of the vertical velocity. Details of the figures are the same as in figure 4. A complete reversal of the flow occurs in the boxed region.

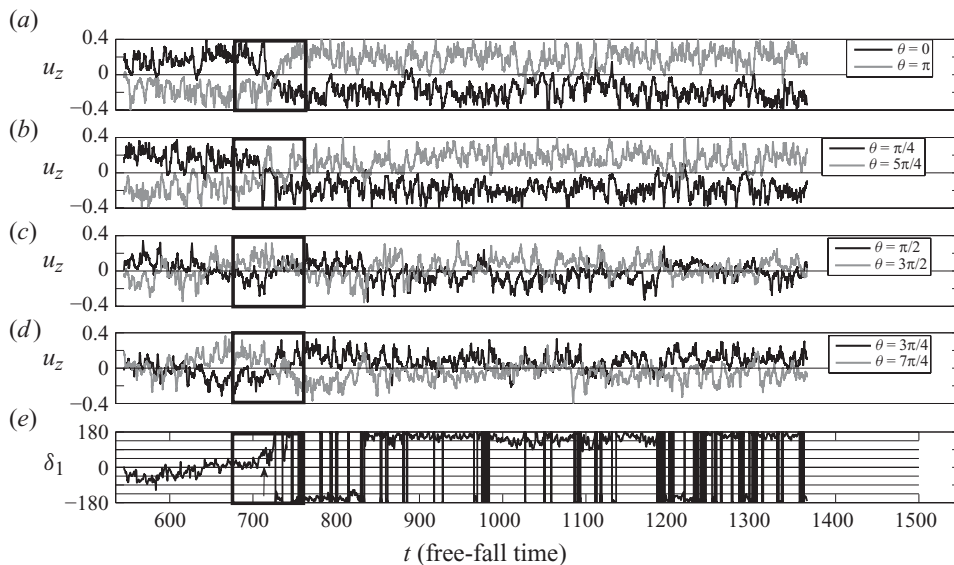


FIGURE 6. For $R = 2 \times 10^7$ on a $100 \times 120 \times 201$ grid, the time series of the vertical velocity measured by the probes at $z = 0.5$ (midplane) and $r = 0.48$, and the phase of the first Fourier mode of the vertical velocity. Details of the figures are the same as in figure 4. A complete reversal of the flow occurs in the boxed region.

where $\theta_j = j\pi/4$ ($j = 0 : 7$), and δ_k is the phase of the k th Fourier mode. Note that the reality condition $\hat{u}_{-k} = \hat{u}_k^*$ is used to derive (3.3). In our simulations, we observe that the first Fourier mode ($k = 1$) dominates over the other modes, except possibly during the reversals. Note that Cioni *et al.* (1997) and Brown & Ahlers (2006) have analysed the properties of $\hat{u}_1(t)$ and $\delta_1(t)$ only using their experimental data. Later, we will compute the amplitudes of the Fourier modes using the vertical velocity fields measured by the probes at $z = 0.5$ and $r = 0.48$.

For a quantitative analysis, Brown *et al.* (2005) and Brown & Ahlers (2006) proposed that the phase of the first Fourier mode δ_1 can be used as an approximate measure for the orientation of the plane of the LSC. Using this criterion, they defined ‘reorientation of the LSC’ as a sudden and significant rotation of the above plane. They used two selection criteria for the reorientation of the LSC: (a) the magnitude of angular change in orientation ($|\Delta\delta_1|$) should be greater $\pi/4$; (b) the azimuthal rotation rate ($|\dot{\delta}_1|$) should be greater than $\pi/(5T_{\text{eddy}})$, where T_{eddy} is the eddy turnover time. We follow the same criteria for the selection of reorientation events in our simulation.

In figures 4–6, we plot the phase of the first Fourier mode (δ_1), which is a measure of the plane of the LSC. Note that the discontinuities from 180° to -180° in the δ_1 diagrams are not reorientations; they simply indicate jitters near 180° . In all the time series of the vertical velocity and the phase of the first Fourier mode, we observe that the mean value of the vertical velocity changes sign but not necessarily simultaneously for all the probes. For example in figure 4, the vertical velocity u_z measured by all the probes reverses sign near $t \simeq 3900$ (the right boxed region of figure 4). This reorientation is a ‘complete reversal’ of the LSC, and it corresponds to a change in δ_1 of around π , i.e. $\Delta\delta_1 \approx \pi$. Near $t \simeq 2700$ (the left boxed region of figure 4) however u_z changes sign for all the probes except at $\theta = 0$ and π . This kind of reorientation will be termed as a ‘partial reversal’, and it corresponds to $\Delta\delta_1 \neq \pi$. Near $t \simeq 2700$, $\Delta\delta_1 \approx 135^\circ$. The time series shown in figures 4–6 exhibit several partial and complete

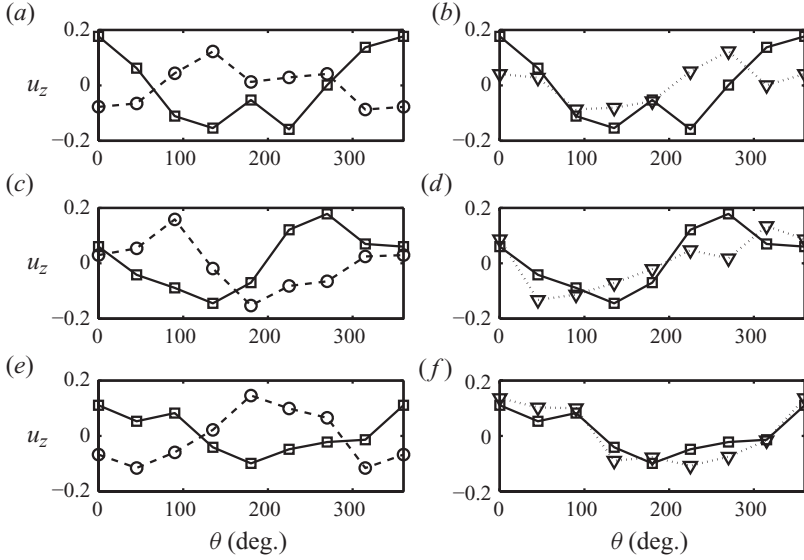


FIGURE 7. Azimuthal profile of the vertical velocity at $z=0.5$ and $r=0.48$ before (solid line) and after the reorientation (dashed line): (a) $R=2 \times 10^7$ at $t=695$ and 750 ; (c) $R=6 \times 10^5$ at $t=2548$ and 2850 ; (e) $R=6 \times 10^5$ at $t=3400$ and 4050 . During the reorientations, the phase of the first Fourier mode changes by $\Delta\delta_1 = 180^\circ$, 135° and 180° , respectively. For the reoriented time series, we subtract $\Delta\delta_1$ from the positive k modes and add $\Delta\delta_1$ to the negative k modes, and construct a modified velocity profile (dotted line). This is shown in (b), (d) and (f), where the reconstructed velocity profiles match quite well with the profiles before the reorientation.

reversals. For example, we observe complete reversals for $R=8 \times 10^6$ and 2×10^7 in the boxed regions shown in these figures.

A careful analysis of the Fourier modes reveals that the complete and partial reversals are intimately related to the change in orientations of the convective structures by $\Delta\delta_1$. We take the real space u_z data before and after the reversals for the three cases shown by arrows in the δ_1 time series in figures 4 and 6. In figure 7(a,c,e) we illustrate the azimuthal profile of the vertical velocity at $z=0.5$ and $r=0.48$ before and after the reorientations by solid and dashed lines, respectively. We calculate $\Delta\delta_1$, the change in the phase of the first Fourier mode, during the reorientations of the structures. If the convective structure rotates by an angle $\Delta\delta_1$ during a reorientation, then, according to (3.3), we can cancel the effects of this reorientation by subtracting $k\Delta\delta_1$ from the phases of all the positive k modes, and by adding $k\Delta\delta_1$ to all the negative k modes of the data recorded after the reorientation (note that the $k=0$ mode is left unaltered). We perform the exercise on the Fourier modes of the data sets recorded after the specified reversals or reorientations. Subsequently, we compute the velocity fields from the modified Fourier coefficients. The modified velocity fields, shown by dotted lines in figure 7(b,d,f), match quite well with the corresponding velocity profiles before the reorientations. Thus, we show that the convective structures essentially rotate by $\Delta\delta_1$ during the reorientations.

The above features of our simulations are in general agreement with the experimental results by Cioni *et al.* (1997), Brown *et al.* (2005), Brown & Ahlers (2006) and Xi *et al.* (2006). Note that the number of reorientations in the convection experiments are much larger than those observed in numerical simulations. In the

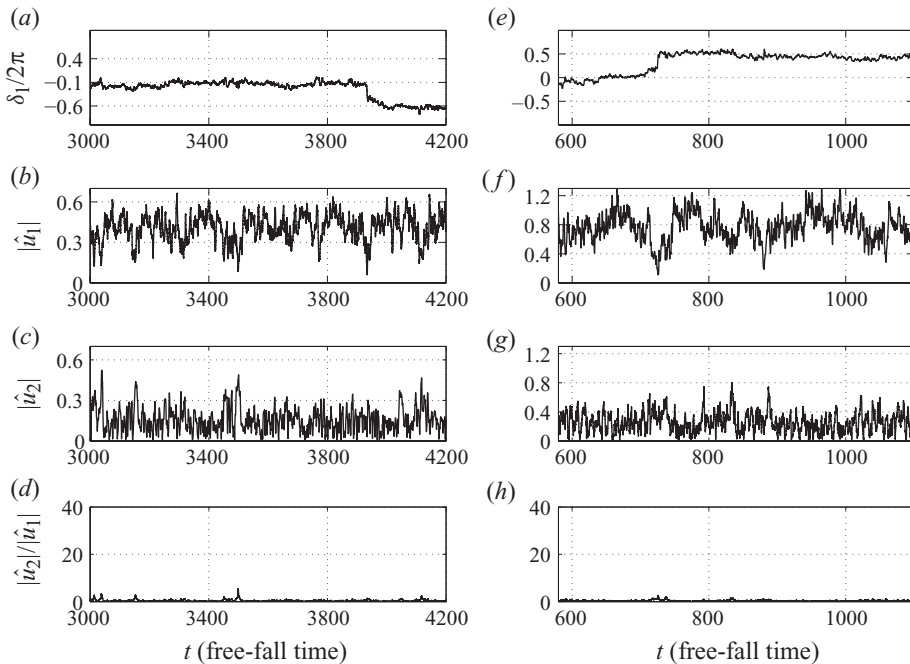


FIGURE 8. Time series of the phase of the first Fourier mode (δ_1) (in units of 2π), amplitude of the first Fourier mode ($|\hat{u}_1|$) and amplitude of the second Fourier mode ($|\hat{u}_2|$) during the rotation-led reversals. (a–d) Time series of δ_1 , $|\hat{u}_1|$, $|\hat{u}_2|$ and $|\hat{u}_2|/|\hat{u}_1|$, respectively, for $R = 6 \times 10^5$ on a $33 \times 49 \times 97$ grid in which the reversal takes place near $t = 3950$. (e–h) Time series of δ_1 , $|\hat{u}_1|$, $|\hat{u}_2|$ and $|\hat{u}_2|/|\hat{u}_1|$ for $R = 2 \times 10^7$ on a $100 \times 120 \times 201$ grid with a reorientation event near $t = 700$.

next section, we analyse the detailed dynamics of the reorientation of the LSC using numerical data.

3.3. Dynamics of reorientations

A careful analysis of the phases and amplitudes of the Fourier modes provides important clues about the dynamics of the reorientations of the LSC and the reversals of the vertical velocity. The amplitudes of the Fourier modes vary significantly over time. We observe that during some of the reversals or reorientations, the amplitude of the first Fourier mode almost vanishes; these reorientations are termed as ‘cessation led’. In the other reorientations that are termed as ‘rotation led’, the Fourier modes continue to fluctuate around their mean values. These kinds of reversals were reported by Brown *et al.* (2005), Brown & Ahlers (2006) and Xi *et al.* (2006) based on their RBC experiment. In the present paper, we probe the dynamics of reversals using numerical simulations.

In figure 8, we plot the phases and amplitudes of the first two Fourier modes during two rotation-led reorientations. For $R = 6 \times 10^5$, figure 8(a) exhibits the time series of the phase ($\delta_1/2\pi$, i.e. in units of 2π). Figure 8(b,c) shows the amplitudes of the first and second Fourier modes ($|\hat{u}_1|$, $|\hat{u}_2|$) respectively, while figure 8(d) shows their ratio $|\hat{u}_2|/|\hat{u}_1|$. As shown in the figures, δ_1 changes by approximately π near $t \approx 3900$, but $|\hat{u}_1|$ and $|\hat{u}_2|$ continue to fluctuate around their average values. However, $|\hat{u}_1|$ always dominates over $|\hat{u}_2|$, as evident from the plot of $|\hat{u}_2|/|\hat{u}_1|$ shown in figure 8(d). Figure 8(e–h) exhibits similar features for $R = 2 \times 10^7$. Note however that $|\hat{u}_1|$ tends

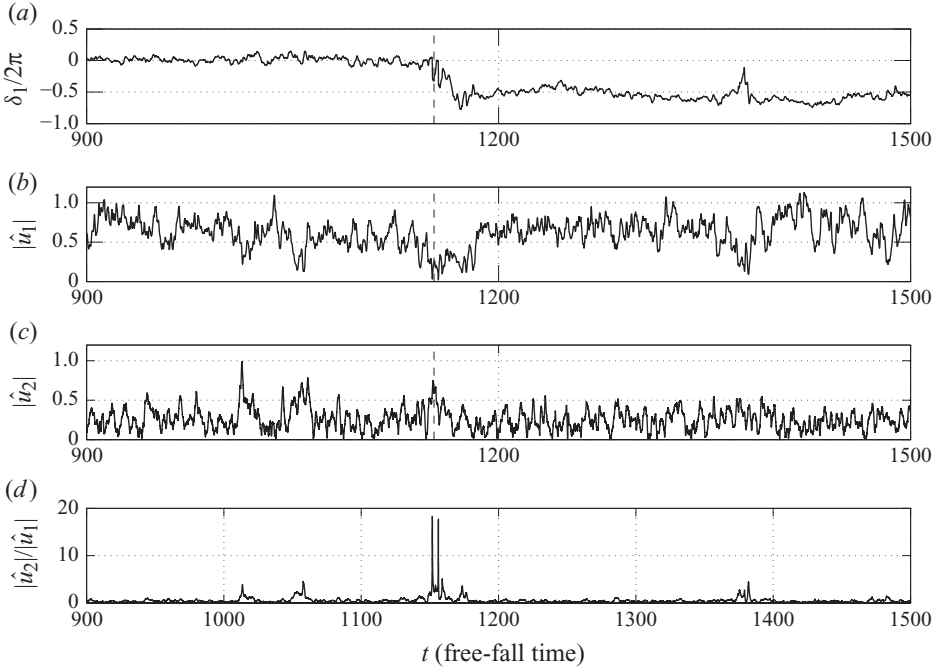


FIGURE 9. (a–d) Time series of δ_1 , $|\hat{u}_1|$, $|\hat{u}_2|$ and $|\hat{u}_2|/|\hat{u}_1|$ indicating a cessation-led reorientation near $t \sim 1175$ for $R = 8 \times 10^6$ ($75 \times 96 \times 145$). The strength of $|\hat{u}_1|$ decreases significantly, while $|\hat{u}_2|/|\hat{u}_1|$ increases during this event.

to have a small dip during the reorientation, but $\Delta|\hat{u}_1|$ is much smaller compared with the cessation-led reversals described later. Note that both these events lead to ‘complete reversals’ since $\Delta\delta_1 \approx \pi$.

In the other set of reversals or reorientations, we observe that the amplitude of the first Fourier mode ($|\hat{u}_1|$) tends to vanish during the event. These sets of reversals were termed as ‘cessation-led’ by Brown *et al.* (2005), Brown & Ahlers (2006) and Xi *et al.* (2006). We illustrate the cessation-led reversals using the following examples.

Figures 9(a) and 9(b) exhibit the time-series plots of δ_1 and $|\hat{u}_1|$, respectively, for $R = 8 \times 10^6$. During the cessation at $t \sim 1175$, $\Delta\delta_1 \approx \pi$ and $|\hat{u}_1|$ tends to zero. The amplitude of the second Fourier mode $|\hat{u}_2|$ however increases slightly above its average value during this event (see figure 9c). The fluctuations in $|\hat{u}_1|$ and $|\hat{u}_2|$ however tend to hide the above features. Therefore, we use $|\hat{u}_2|/|\hat{u}_1|$ to amplify the decrease in $|\hat{u}_1|$ and increase in $|\hat{u}_2|$ to be able to identify the cessation-led reversals clearly. In figure 9(d), we plot $|\hat{u}_2|/|\hat{u}_1|$, which exhibits a sharp peak during the event. This is an example of the cessation-led complete reversal since $\Delta\delta_1 \approx \pi$. Figure 10 shows the corresponding quantities for another set of cessation-led reorientations for $R = 6 \times 10^5$. As evident from the time series, near $t \sim 6620$, $\Delta\delta_1 \sim (3.2 - 2)2\pi \approx 72^\circ$. Later at $t \sim 6720$, $\Delta\delta_1 \sim (2 - 1.2)2\pi \approx -72^\circ$. These two reorientations of figure 10 are partial ones, and the LSC returns to its original configuration after the two reorientations ($\Delta\delta_1 = (3.2 - 1.2)2\pi$). During both these events, $|\hat{u}_2|/|\hat{u}_1|$ has a sharp peak.

In our simulations, we also observe reorientations involving ‘double cessations’, first observed by Xi *et al.* (2006) in their experiments. During these events, the phase δ_1 changes in two stages in quick succession, first by θ_1 and second by θ_2 . Therefore, the

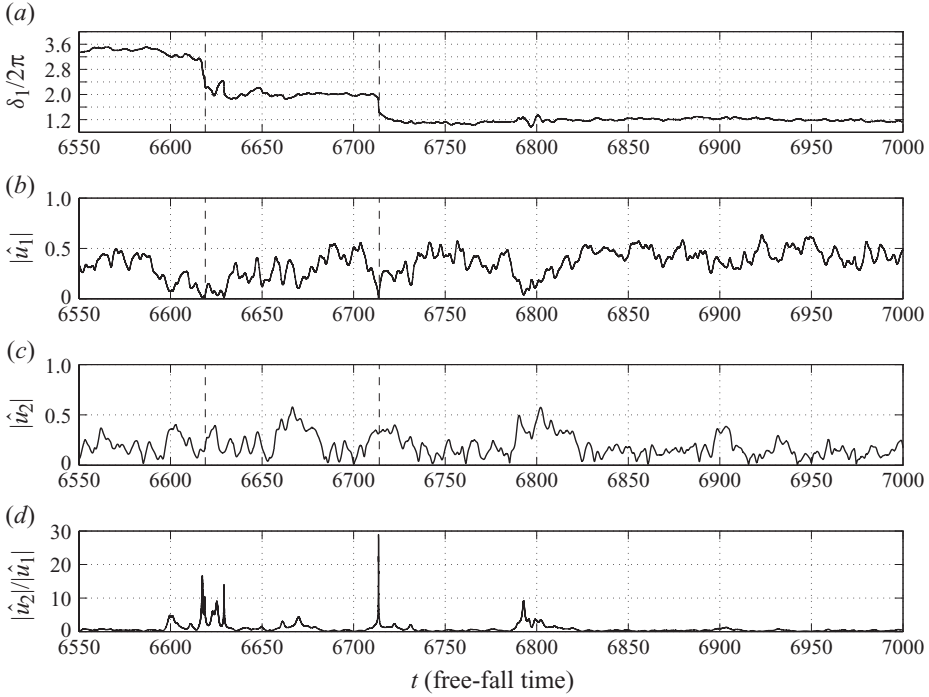


FIGURE 10. (a–d) Time series of δ_1 , $|\hat{u}_1|$, $|\hat{u}_2|$ and $|\hat{u}_2|/|\hat{u}_1|$ indicating cessation-led partial reorientations near $t \sim 6625$ and 6710 for $R = 6 \times 10^5$ ($33 \times 49 \times 97$ grid). For both the events $\Delta\delta_1$ is approximately 72° .

net $\Delta\delta_1 \approx \theta_1 + \theta_2$. During double cessation, $|\hat{u}_1|$ vanishes on two occasions separated by a small time gap (within an eddy turnover time). Note that $|\hat{u}_2|$ tends to increase during these times; hence, $|\hat{u}_2|/|\hat{u}_1|$ exhibits two peaks within a short time interval. Two independent double-cessation events have been illustrated in figures 11(a) and 12(a) (for $R = 6 \times 10^5$). In figure 11(a), we observe the first cessation at $t \approx 2083$, followed by the second cessation at $t \approx 2088$, and $\theta_1 \approx -\theta_2 \approx \pi$. In figure 12(a), the first cessation occurs at $t \approx 2464$, followed by the second cessation at $t \approx 2466$ with $\theta_1 \approx -\theta_2 \approx 0.8\pi$. Since the net change in the phase δ_1 is approximately zero, the final configuration of the LSC is similar to its original configuration. Note that one eddy turnover time for the corresponding run is approximately 26 free-fall times (see table 2). Hence, the two double cessations occur within 0.2 and 0.08 eddy turnover time, respectively, which is consistent with the experimental result of Xi *et al.* (2006).

For $R = 6 \times 10^5$, we observe two events that are similar to the above-mentioned double-cessation events (see figure 13a–d). Near $t \approx 4540$, δ_1 changes twice, $\theta_1 \approx 0.6\pi$ and $\theta_2 \approx -0.6\pi$ with net $\Delta\delta_1 \approx 0$. These two events however occur very close to each other, and we observe only one peak for $|\hat{u}_2|/|\hat{u}_1|$, rather than any double peaks indicative of double cessation. Another cessation-led reorientation occurs near $t \approx 4270$, which resembles the above-mentioned double-cessation event except for one major difference. Here $\theta_1 \approx 0.8\pi$ and $\theta_2 \approx -0.6\pi$; hence, the LSC reorients by a net angle after the event. Note that for the double-cessation reported by Xi *et al.* (2006), $\theta_1 \approx -\theta_2$ and the net change in δ_1 is zero. In our numerical simulations, we find such events. In addition, we also observe a double cessation where $\theta_1 \neq -\theta_2$, and the LSC reorients by a finite angle after the event.

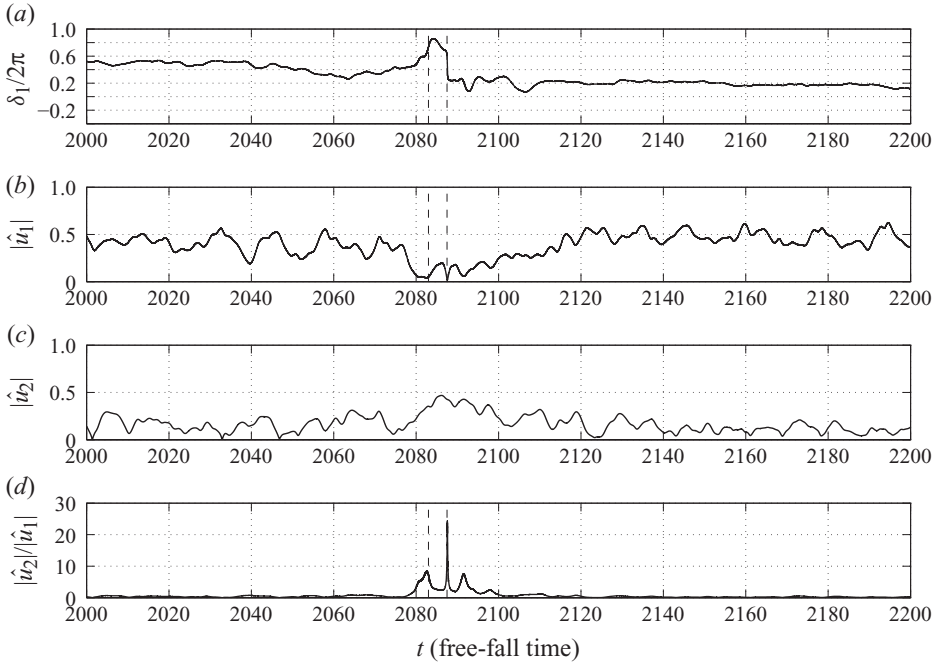


FIGURE 11. (a–d) Time-series plot of δ_1 , $|\hat{u}_1|$, $|\hat{u}_2|$ and $|\hat{u}_2|/|\hat{u}_1|$ indicating double cessation for $R = 6 \times 10^5$ ($33 \times 49 \times 97$ grid). The first cessation occurs at $t \sim 2083$ and the second at $t \sim 2088$. During both the events, $|\hat{u}_1|$ becomes weak and $|\hat{u}_2|$ dominates. In (d), the two spikes in $|\hat{u}_2|/|\hat{u}_1|$ during the events are shown.

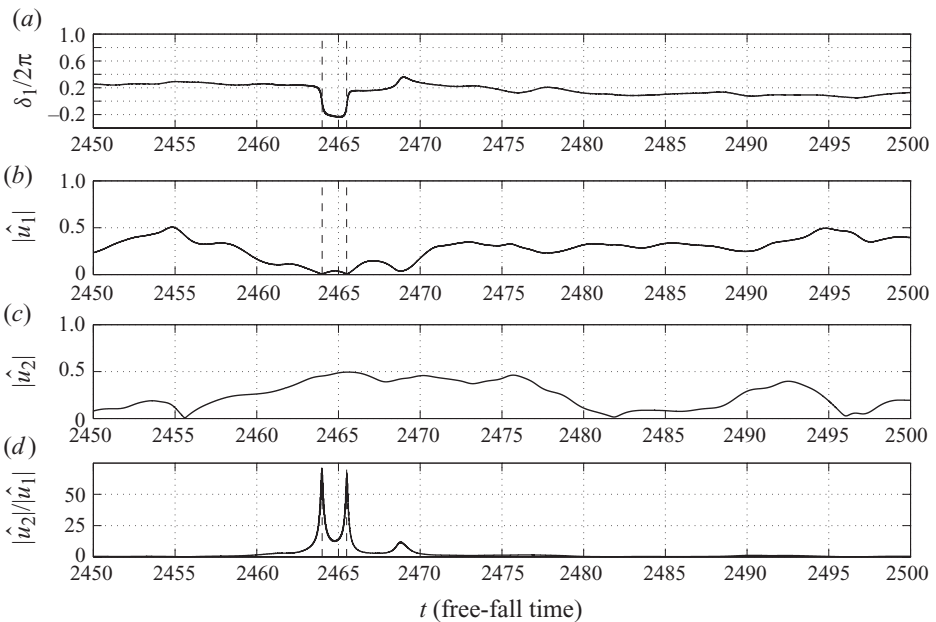


FIGURE 12. (a–d) Time-series plot of δ_1 , $|\hat{u}_1|$, $|\hat{u}_2|$ and $|\hat{u}_2|/|\hat{u}_1|$ indicating double cessation for $R = 6 \times 10^5$ ($33 \times 49 \times 97$ grid). The first cessation at $t \sim 2464$ is followed by the second at $t \sim 2466$. During both the events, $|\hat{u}_1|$ becomes weak and $|\hat{u}_2|$ dominates. In (d), the two spikes in $|\hat{u}_2|/|\hat{u}_1|$ during the events are shown.

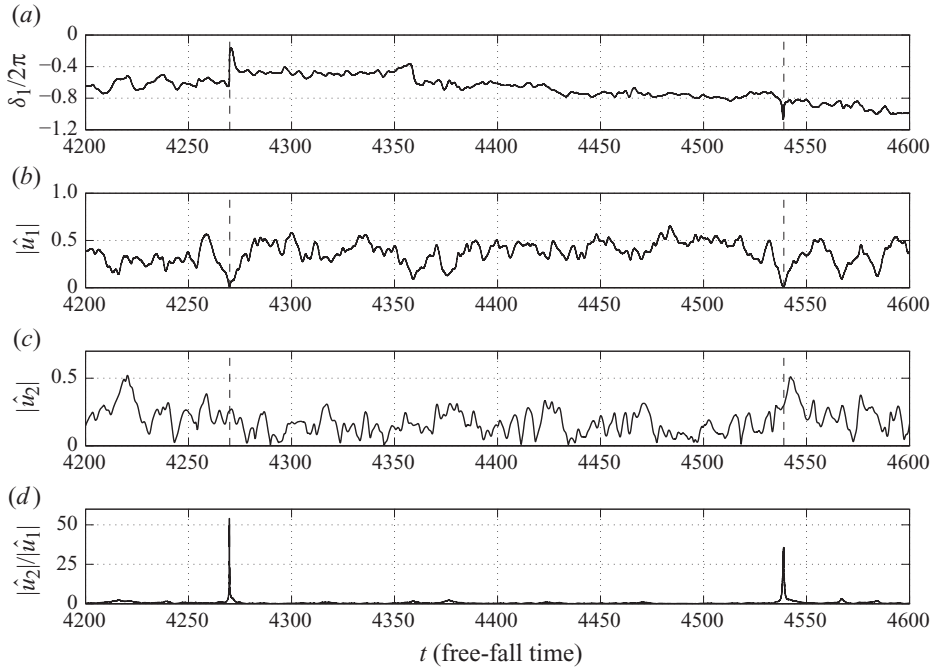


FIGURE 13. (a–d) For $R = 6 \times 10^5$ time-series plot of δ_1 , $|\hat{u}_1|$, $|\hat{u}_2|$ and $|\hat{u}_2|/|\hat{u}_1|$ depicting events similar to double cessations ($33 \times 49 \times 97$ grid). $\Delta\delta_1 \sim 72^\circ$ near $t \sim 4270$, while $\Delta\delta_1 \approx 0$ near $t \sim 4540$. During both the events, $|\hat{u}_1| \rightarrow 0$ but the ratio $|\hat{u}_2|/|\hat{u}_1|$ increases significantly.

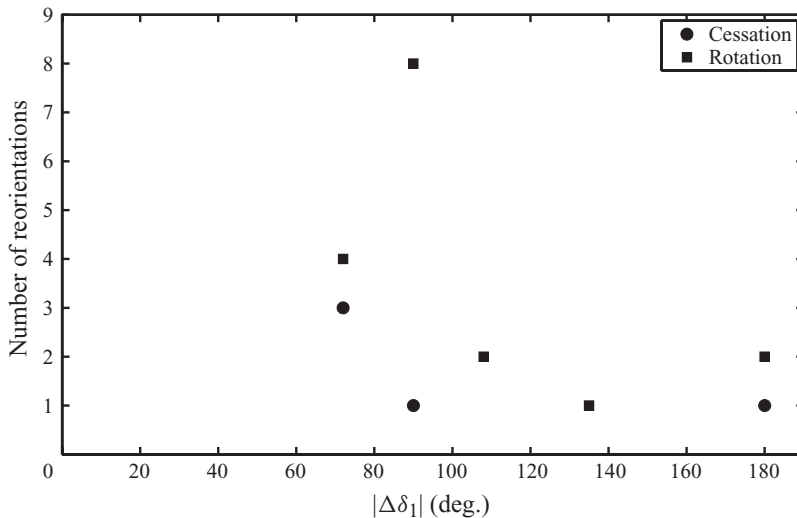


FIGURE 14. The distribution of the change in the phase of the first Fourier mode ($|\Delta\delta_1|$) of the LSC during reorientations. Criteria of Brown *et al.* (2005) and Brown & Ahlers (2006) have been used for identifying reorientations of the LSC.

Figure 14 illustrates the distribution of $\Delta\delta_1$ of the LSC observed in our numerical simulations. We observe three complete reorientations ($\Delta\delta_1 \approx \pi$), two rotation-led and one cessation-led. The number of observed partial reorientations is rather large (19). Of these partial reorientation events, 15 are rotation-led while four are

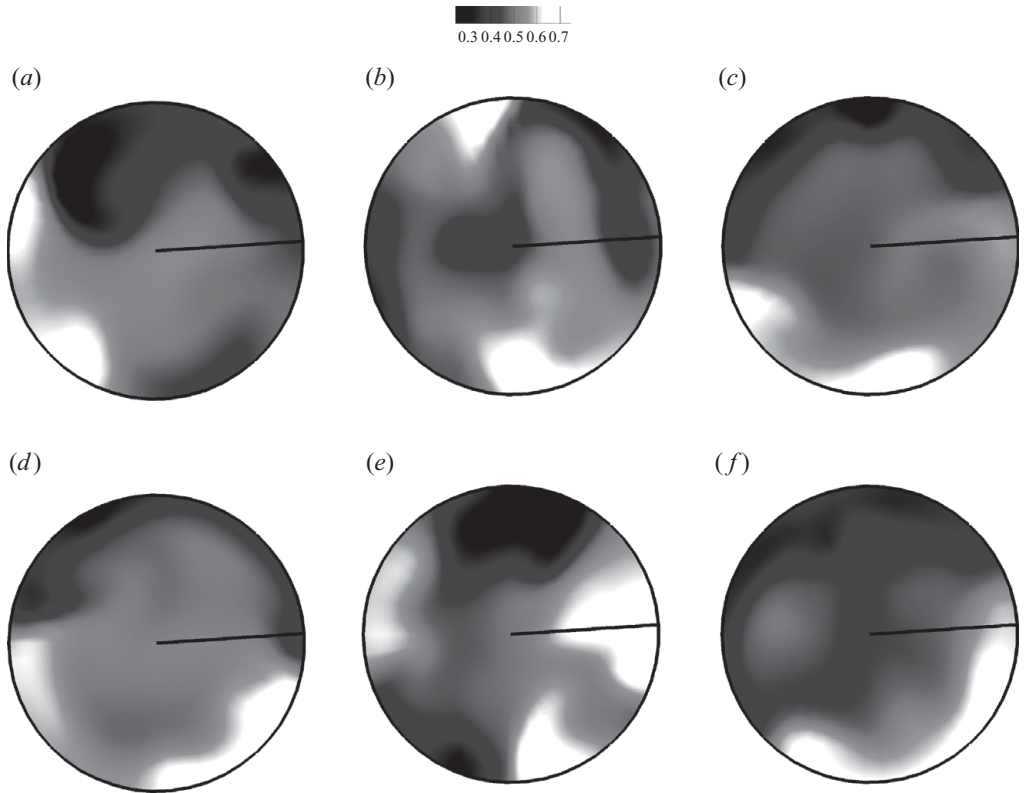


FIGURE 15. Temperature snapshots at the midplane ($z=0.5$) during cessation-led reorientations near $t \sim 2087$ (a–c) and 4539 (d–f) for $R = 6 \times 10^5$. Dipolar structures are dominant before and after the reorientations, but the quadrupolar structure is prominent during the reorientations (at $t = 2087$ and 4539). The horizontal solid lines provide a guide for the azimuthal reorientations of the convective structure. In (a–f), $t = 2053, 2087, 2125, 4500, 4539, 4556$, respectively.

cessation-led. We also observe four double cessations, three of them have $\Delta\delta_1 \approx 0$ while one has $\Delta\delta_1 \approx 0.2\pi$. These observations indicate that cessation-led events are rarer compared with the rotation-led events, an observation consistent with that of Brown *et al.* (2005) and Brown & Ahlers (2006). The number of reorientations observed in our simulations are far fewer compared with those observed by Brown *et al.* (2005), Brown & Ahlers (2006), Cioni *et al.* (1997) and Xi *et al.* (2006). Consequently, we are unable to perform statistics of reorientations similar to those by Brown *et al.* (2005) and Brown & Ahlers (2006).

In our numerical simulations, we observe that the higher Fourier modes play an interesting role during reorientations. These kinds of investigations were missing in earlier experimental works. We find that during the cessation-led reorientations, $|\hat{u}_2|$ tends to become significant when $|\hat{u}_1|$ tends to vanish. This feature is evident from the significant increase in the magnitude of $|\hat{u}_2|/|\hat{u}_1|$ during the cessation-led reorientations. Brown *et al.* (2005) and Brown & Ahlers (2006) interpret such events as cessation of the circulation, followed by a restart in a randomly chosen new direction. Our simulation results are consistent with the above interpretation, yet another scenario is also possible. During the cessation, the circulation structure corresponding to \hat{u}_1 (dipolar in a horizontal plane) becomes very weak, and the quadrupole structure

corresponding to \hat{u}_2 becomes dominant. After the cessation, the quadrupole structure disappears and the dipolar structure reappears with a shift in the azimuthal direction. These features have been illustrated in figure 15, in which we show the horizontal profile of temperature in the $z=0.5$ plane before, during and after two cessation-led reorientations for $R=6 \times 10^5$. Figure 15(a–c) represents the temperature snapshots near a double-cessation event (near $t=2100$ in figure 11). The system starts from the \hat{u}_1 dominant state with approximate profile as $\cos(\theta + \delta_1)$ of figure 15(a). During the cessation, the system profile appears as in figure 15(b), which has \hat{u}_2 as the most prominent Fourier mode with profile as $\cos(2\theta + \delta_2)$. After the double cessation, the system returns to the \hat{u}_1 dominant structure, as evident from figure 15(c). Similar features are observed for another cessation-led reorientation near $t \approx 4500$ for $R=6 \times 10^5$ shown in figure 15(d–f). Note that in the rotation-led reorientations, the dipolar structure continues to be dominant during the reorientation itself.

In this section, we have presented some of the complex dynamics of the reorientations of the LSC. The reversals of the vertical velocity have been shown to be intimately related to the reorientations of the LSC. We observe rotation-led and cessation-led reorientations, which were first reported by Brown *et al.* (2005) and Brown & Ahlers (2006) and later observed in other experiments (Xi *et al.* 2006; Xi & Xia 2007, 2008b). In our simulations, we also find double cessation, previously observed by Xi *et al.* (2006). A new feature of our simulations is a double cessation in which the orientation of the LSC after the event is different from the original orientation. In our analysis, we study higher Fourier modes, notably \hat{u}_2 , which was missing in earlier work on reversals. We propose a new interpretation of the cessation-led reorientations and argue that the LSC transforms from a dipolar (\hat{u}_1 dominant) to quadrupolar (\hat{u}_2 dominant), and then back to dipolar (\hat{u}_1 dominant) structure during this event.

4. Summary and conclusions

In summary, we numerically compute turbulent convective flows for a cylindrical geometry and study the characteristics of the LSC, in particular those related to flow reversals. The first Fourier mode along the azimuthal direction is the most dominant mode; the phase of this mode (δ_1) is used as a measure of the orientation of the LSC. Our numerical results and earlier experimental results indicate that the LSC occasionally reorients itself by rotating in the azimuthal direction by an arbitrary angle. When the reorientation angle is around π , the vertical velocity at *all* probes changes sign, signalling complete reversal of the flow. A partial reversal is observed when the reorientation angle is less than π . We therefore argue that the primary cause of the flow reversal is the azimuthal reorientation of the LSC.

In our numerical simulations, we observe two kinds of reorientations, rotation-led and cessation-led, earlier observed by Brown *et al.* (2005), Brown & Ahlers (2006) and Xi *et al.* (2006). The rotation-led reversals involve rotation of the LSC without appreciable reduction in circulation strength, i.e. the amplitude of $|\hat{u}_1|$ remains finite. In the cessation-led reversals, $|\hat{u}_1| \rightarrow 0$, which is interpreted by Brown *et al.* (2005) and Brown & Ahlers (2006) as cessation of circulation followed by a restart in a randomly chosen new direction. During this event, our numerical simulations reveal that the ratio of the amplitude of the second and first Fourier modes, i.e. $|\hat{u}_2|/|\hat{u}_1|$, increases significantly and then returns to its original level. These properties of the Fourier modes reveal that during the cessation, the LSC transforms from a dipolar-like structure to a quadrupolar-like structure, and then back to a dipolar-like structure.

These features appear to have certain similarities with the reversals of a magnetic field in a dynamo (Wicht & Olson 2004). The role of higher Fourier modes in reversals and reorientations of the LSC has been highlighted in our simulations for the first time.

We also observe double cessation in our simulations. Xi *et al.* (2006) had observed in their experiments that the LSC returns to its original orientation (approximately) after a double cessation. We however find that the change in the orientations of the LSC during some double cessations is zero, while in some others, the changes are non-zero.

Our numerical simulations reproduced many features (e.g. ‘rotation-led reorientations’, ‘cessation-led reorientations’ and ‘double cessation’) observed in convection experiments by Cioni *et al.* (1997), Brown *et al.* (2005), Brown & Ahlers (2006), Xi *et al.* (2006) and Niemela *et al.* (2001) for Rayleigh numbers greater than those in our simulations. Several researchers have argued that the reorientations, including reversals, of LSC occur only under strong turbulence regimes (say $R > 10^8$). We however observe that the nature of convective flows and reorientations is very similar for the range of Rayleigh numbers studied by us ($R = 6 \times 10^5$ to $R = 3 \times 10^7$). The lowest Rayleigh number $R = 6 \times 10^5$ is probably in the weak turbulence regime where the LSC is not well organized and $R = 3 \times 10^7$ is in the lower end of the strong turbulence regime. We could not carry out simulations for even larger Rayleigh numbers due to very expensive computational requirements for these runs. However, we believe that reversals in high-Rayleigh-number regimes are highly likely to be similar to those presented in the simulations.

We thank Krishna Kumar, Stéphan Fauve, K. R. Sreenivasan, J. J. Niemela, Pankaj Wahi, Supriyo Paul and Pinaki Pal for very useful discussions and comments. We also thank the reviewers who provided many useful comments, interesting ideas and suggestions that have contributed significantly to the improvement of the paper. This work was supported by a research grant by the Department of Science and Technology, India, as Swarnajayanti fellowship to M.K.V.

Supplementary movies are available at journals.cambridge.org/flm.

REFERENCES

- AHLERS, G., GROSSMANN, S. & LOHSE, D. 2009 Heat transfer and large-scale dynamics in turbulent Rayleigh–Bénard convection. *Rev. Mod. Phys.* **81**, 503–537.
- ARAUJO, F. F., GROSSMANN, S. & LOHSE, D. 2005 Wind reversals in turbulent Rayleigh–Bénard convection. *Phys. Rev. Lett.* **95**, 084502.
- BENZI, R. 2005 Flow reversal in a simple dynamical model of turbulence. *Phys. Rev. Lett.* **95**, 024502.
- BENZI, R. & VERZICCO, R. 2008 Numerical simulations of flow reversal in Rayleigh–Bénard convection. *Europhys. Lett.* **81**, 64008.
- BREUER, M. & HANSEN, U. 2009 Turbulent convection in the zero Reynolds number limit. *Europhys. Lett.* **86**, 24004.
- BROWN, E. & AHLERS, G. 2006 Rotations and cessations of the large-scale circulation in turbulent Rayleigh–Bénard convection. *J. Fluid Mech.* **568**, 351–386.
- BROWN, E. & AHLERS, G. 2007 Large-scale circulation model for turbulent Rayleigh–Bénard convection. *Phys. Rev. Lett.* **98**, 134501.
- BROWN, E. & AHLERS, G. 2008 A model of diffusion in a potential well for the dynamics of the large-scale circulation in turbulent Rayleigh–Bénard convection. *Phys. Fluids* **20**, 075101.
- BROWN, E., FUNFSCHILLING, D. & AHLERS, G. 2007 Anomalous Reynolds-number scaling in turbulent Rayleigh–Bénard convection. *J. Stat. Mech.* **10**, P10005.

- BROWN, E., NIKOLAENKO, A. & AHLERS, G. 2005 Reorientation of the large-scale circulation in turbulent Rayleigh–Bénard Convection. *Phys. Rev. Lett.* **95**, 084503.
- CASTAING, B., GUNARATNE, G., HESLOT, F., KADANOFF, L., LIBCHABER, A., THOMAE, S., WU, X-Z., ZALESKI, S. & ZANETTI, G. 1989 Scaling of hard thermal turbulence in Rayleigh–Bénard convection. *J. Fluid Mech.* **204**, 1–30.
- CIONI, S., CILIBERTO, S. & SOMMERIA J. 1997 Strongly turbulent Rayleigh–Bénard convection in mercury: comparison with results at moderate Prandtl number. *J. Fluid Mech.* **335**, 111–140.
- GRÖTZBACH, G. 1983 Spatial resolution requirement for direct numerical simulation of Rayleigh–Bénard convection. *J. Comput. Phys.* **49**, 241–264.
- HANSEN, U., YUEN, D. A. & KROENING, S. E. 1990 Transition to hard turbulence in thermal convection at infinite Prandtl number. *Phys. Fluids A* **2** (12), 2157–2163.
- HANSEN, U., YUEN, D. A. & KROENING, S. E. 1992 Mass and heat transport in strongly time-dependent thermal convection at infinite Prandtl number. *Geophys. Astrophys. Fluid Dyn.* **63**, 67.
- KADANOFF, L. P. 2001 Turbulent heat flow: structures and scaling. *Phys. Today* **54**, 34–39.
- KRISHNAMURTI, R. & HOWARD, L. N. 1981 Large-scale flow generation in turbulent convection. *Proc. Natl Acad. Sci. USA* **78**, 1981–1985.
- NIEMELA, J. J. *et al.* 2000 Turbulent convection at very high Rayleigh numbers. *Nature (London)* **404**, 837–840.
- NIEMELA, J. J., SKRBEK, L., SREENIVASAN, K. R. & DONNELLY, R. J. 2001 The wind in confined thermal convection. *J. Fluid Mech.* **449**, 169–178.
- PAUL, S., KUMAR, K., VERMA, M. K., CARATI, D., DE, A. & ESWARAN, V. 2010 Chaotic travelling rolls in Rayleigh–Bénard convection. *Pramana* **74**, 75–82.
- QIU, X. L. & TONG, P. 2001 Onset of coherent oscillations in turbulent Rayleigh–Bénard convection. *Phys. Rev. Lett.* **87**, 094501.
- SANO, M., WU, X. Z. & LIBCHABER, A. 1989 Turbulence in helium gas free convection. *Phys. Rev. A* **40**, 6421–6430.
- SHRAIMAN, B. I. & SIGGIA, E. D. 1990 Heat transport in high-Rayleigh number convection. *Phys. Rev. A* **42**, 3650–3653.
- SREENIVASAN, K. R., BERSHADSKII, A. & NIEMELA, J. J. 2002 Mean wind and its reversal in thermal convection. *Phys. Rev. E* **65**, 056306.
- STEVENS, R. J. A. M., VERZICCO, R. & LOHSE D. 2010 Radial boundary layer structure and Nusselt number in Rayleigh–Bénard convection. *J. Fluid Mech.* **643**, 495–507.
- STRINGANO, G. & VERZICCO, R. 2006 Mean flow structure in thermal convection in a cylindrical cell of aspect ratio one half. *J. Fluid Mech.* **548**, 1–16.
- TAM, C. K. W. & WEBB, J. C. 1993 Dispersion-relation-preserving finite difference schemes for computational acoustic. *J. Comput. Phys.* **107**, 262–281.
- TSUJI, Y., MIZUNO, T., MASHIKO, T. & SANO, M. 2005 Mean wind in convective turbulence of mercury. *Phys. Rev. Lett.* **94**, 034501.
- VERZICCO, R. & CAMUSSI, R. 1999 Prandtl number effects in convective turbulence. *J. Fluid Mech.* **383**, 55–73.
- VILLERMAUX, E. 1995 Memory-induced low frequency oscillations in closed convection boxes. *Phys. Rev. Lett.* **75**, 4618.
- WICHT, J. & OLSON, P. 2004 A detailed study of the polarity reversal mechanism in a numerical dynamo model. *Geochem. Geophys. Geosyst.* **5**, Q03H10.
- XI, H. D., LAM, S. & XIA, K. Q. 2004 From laminar plumes to organized flows: the onset of large-scale circulation in turbulent thermal convection. *J. Fluid Mech.* **503**, 47–56.
- XI, H. D. & XIA, K. Q. 2007 Cessations and reversals of the large-scale circulation in turbulent thermal convection. *Phys. Rev. E* **75**, 066307.
- XI, H. D. & XIA, K. Q. 2008*a* Flow mode transitions in turbulent thermal convection. *Phys. Fluids* **20**, 055104.
- XI, H. D. & XIA, K. Q. 2008*b* Azimuthal motion, reorientation, cessation, and reversal of the large-scale circulation in turbulent thermal convection: a comparative study in aspect ratio one and one-half geometries. *Phys. Rev. E* **78**, 036326.
- XI, H. D., ZHOU, Q. & XIA, K. Q. 2006 Azimuthal motion of the mean wind in turbulent thermal convection. *Phys. Rev. E* **73**, 056312.